Editors' Suggestion | Featured in Physics

Altermagnetic Proximity Effect

Ziye Zhu,[1] Richang Huang,[1] Xianzhang Chen,[1] Zhou Cui,[1] Xunkai Duan,[1] Jiayong Zhang,[1,2] Igor Žutić,[3] and Tong Zhou[1,*]

[1]Ningbo Institute of Digital Twin, Eastern Institute of Technology, Ningbo, Zhejiang 315200, China
[2]School of Physical Science and Technology, Suzhou University of Science and Technology, Suzhou, 215009, China
[3]Department of Physics, University at Buffalo, State University of New York, Buffalo, New York 14260, USA

(Received 8 September 2025; revised 22 December 2025; accepted 9 March 2026; published 5 May 2026)

Proximity effects complement conventional materials design by enabling interfacial properties absent in any constituent. Here, we uncover an altermagnetic proximity effect (AMPE), distinct from ferromagnetic and antiferromagnetic proximity, in which the hallmark momentum-alternating spin splitting of an altermagnet is transferred across an interface into an adjacent nonmagnetic layer—a process we term "altermagnetization." Using first-principles calculations and model analysis, we identify the AMPE in heterostructures based on the prototypical van der Waals altermagnet V_2Se_2O, where a proximitized monolayer PbO acquires altermagnetic band splitting and real-space spin textures, with systematic tunability via interlayer spacing and magnetic configuration. We further demonstrate that the AMPE enables valley-dependent spin splitting in the semiconductor PbS and realizes topological superconductivity in the *s*-wave superconductor $NbSe_2$, both inheriting the altermagnetic spin texture. Finally, we validate the generality and experimental feasibility of the AMPE by realizing it in a broader class of established altermagnets, including V_2Se_2O derivatives, Ruddlesden-Popper perovskites, and the metallic CrSb. Our results identify the AMPE as a universal proximity mechanism and a versatile platform for engineering emergent quantum phenomena in heterostructures.

DOI: 10.1103/kqy8-myz1

Proximity effects allow a material to acquire properties of its neighbors, becoming magnetic, superconducting, topologically nontrivial, or exhibiting enhanced spin-orbit coupling [1–3]. Magnetic proximity effects, particularly in ferromagnets, are widely used to generate spin splitting and tune magnetic parameters that include anisotropy, coercivity, and exchange bias [3–11]. Antiferromagnetic proximity, in turn, relies on interfacial hybridization without fringing fields, enabling ultrafast spin dynamics and symmetry-enforced transport [1,12,13]. These mechanisms underpin modern spintronics, valleytronics, topological states, and heterostructures of superconductors and magnets [14–19].

A growing class of unconventional magnets [20–28], often termed altermagnets (AMs) [29–40], exhibits properties beyond common ferromagnets and antiferromagnets, most notably momentum-dependent alternating spin splitting without net magnetization. This nonrelativistic spin splitting and its tunability expand the opportunities in spintronics [41–45], multiferroics [46–56], topotronics [57–62], and superconductivity [63–68]. A central challenge now lies in understanding if this distinctive magnetic order, rooted in antiferromagnetic (AFM) sublattices linked by symmetries involving rotations [29–32] can be transferred across an interface into otherwise nonmagnetic (NM) layers. Establishing whether AMs generate a distinct proximity effect, rather than simply mimicking ferromagnetic or antiferromagnetic proximity, is key to assessing their impact. Equally important is clarifying if this proximity channel can enable unexplored phenomena, particularly in van der Waals (vdW) heterostructures, where proximity effects are most tunable [69–73].

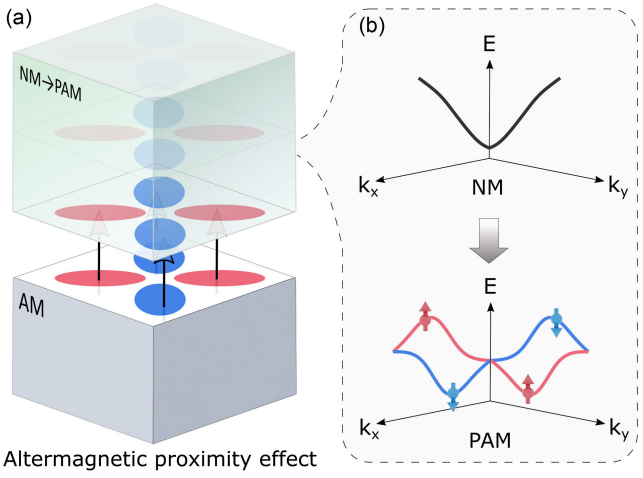

FIG. 1. Schematic of the AMPE. (a) Altermagnetism penetrating an NM layer. (b) Band evolution of the NM layer as it becomes a PAM.

*Contact author: tzhou@eitech.edu.cn

In this Letter, we address these questions by introducing the altermagnetic proximity effect (AMPE) as in Fig. 1 in which the momentum-alternating spin splitting intrinsic to AMs is imprinted onto a neighboring nonmagnetic layer through an interfacial process we term "altermagnetization." Combining first-principles calculations with model analysis, we establish the AMPE in heterostructures formed from the prototypical altermagnetic V_2Se_2O and monolayer PbO: the PbO layer becomes altermagnetized, as evidenced by the induced altermagnetic band splitting and real-space spin densities, whose systematic evolution with interlayer spacing and magnetic configuration demonstrates both robustness and tunability of the AMPE. We then illustrate broader consequences of this effect by showing that the AMPE can generate valley-dependent spin splitting in PbS and enable a topological superconductivity in $NbSe_2$. Finally, by extending our analysis beyond the V_2Se_2O platform to additional altermagnetic classes, including V_2Se_2O derivatives, Ruddlesden-Popper perovskites, and the metallic CrSb, we establish the AMPE as a distinct and universal proximity mechanism and a viable route for engineering multifunctional quantum states in heterostructures.

Our proposed AMPE is schematically illustrated in Fig. 1(a). When an NM material is placed in contact with an altermagnet, the extension of electronic wave functions across the interface can imprint the characteristic alternating spin splitting of the AM onto the NM layer. This interfacial process drives a transition from the NM state to a proximitized altermagnet (PAM), in which originally spin-degenerate bands acquire momentum-dependent spin polarization [Fig. 1(b)]. As with other proximity effects [1], the AMPE is short ranged and decays with distance from the interface. Two-dimensional vdW systems, with atomically thin layers and clean interfaces, thus provide an ideal platform to exploit this AMPE and to design the corresponding highly tunable functionalities.

While most experimentally confirmed AMs exist as bulk crystals or thin films [33–36], V_2Se_2O stands out as a famous vdW candidate [26,74]. Its intercalated metallic derivatives have also been experimentally identified as AMs [35,36], further highlighting its versatility. V_2Se_2O crystallizes in a square lattice where the two V sublattices form a checkerboard AFM configuration linked by C_{4z} symmetry [Fig. 2(a)]. This symmetry yields the hallmark AM features, as confirmed by our calculations showing alternating spin densities in real space and momentum-dependent spin splitting [Fig. 2(c)]. To demonstrate the AMPE of V_2Se_2O, we select PbO as the adjacent NM layer. PbO is a well-established semiconductor with a simple, well-characterized crystal structure and spin-degenerate bands [75,76], as shown in our calculations [Fig. 2(b)]. Importantly, PbO and V_2Se_2O both form 2D square lattices with a minimal lattice mismatch of just 0.7%, making PbO an ideal and clean reference to isolate and analyze the AMPE from V_2Se_2O.

To investigate the emergence of the AMPE, we computed the total energies of several stacking configurations of the PbO/V_2Se_2O heterostructure (see Supplemental Material [77]) and identified the most stable arrangement shown in Fig. 2(a). The corresponding band structure [Fig. 2(d)] indicates that both constituents largely preserve their intrinsic electronic features under vdW coupling. Strikingly, however, the PbO layer now exhibits pronounced momentum-dependent spin splitting [Figs. 2(d)–2(f)], in sharp contrast to its pristine spin-degenerate state [Fig. 2(b)], demonstrating that PbO is transformed into a PAM-PbO through AMPE. The induced spin splitting displays a characteristic altermagnetic signature: spin degeneracy is preserved along $\Gamma - M$, while opposite spin polarizations appear along $M - X - \Gamma$ and $\Gamma - Y - M$, consistent with the underlying order of V_2Se_2O. Moreover, the real-space spin density of PAM-PbO mirrors the symmetry of the V_2Se_2O substrate, providing direct evidence that PbO inherits the altermagnetic character of V_2Se_2O. To confirm this, we further convert V_2Se_2O into a conventional AFM configuration by rearranging its spin sublattices [Fig. 2(i); see Supplemental Material [77]]. In this case, the sublattices are related by translation or inversion symmetry, eliminating the alternating spin splitting. As expected, the induced splitting in PbO disappears [Fig. 2(i)], while its spin density develops an AFM feature, indicating a conventional AFM proximity effect. This control case further illustrates the AMPE of V_2Se_2O.

To further elucidate how PbO is influenced by the AMPE of V_2Se_2O, we analyze the interfacial interaction and charge redistribution in their vdW heterostructure. The planar-averaged charge density difference $\Delta q(z)$, together with the real-space redistribution shown in Fig. 2(g), indicates a slight interfacial charge transfer from PbO to V_2Se_2O. Such a modest charge transfer has a negligible effect on the altermagnetic ground state of V_2Se_2O, as further corroborated by the doping simulations in Supplemental Material [77]. Because the strength of proximity effects is highly sensitive to interlayer spacing, we evaluate the evolution of the spin splitting ΔE_S as a function of the separation d between PbO and V_2Se_2O. As shown in Fig. 2(h), the induced ΔE_S decreases monotonically with increasing d, accompanied by a corresponding reduction of the spin density, confirming the short-range nature of the AMPE. Taken together, these results provide unambiguous evidence for the AMPE from multiple, mutually consistent perspectives.

Valleytronics—Beyond charge and spin, the valley degree of freedom provides a powerful route toward valleytronic devices and robust topological states [15,83–86]. A common strategy to lift valley degeneracy is to apply an external magnetic field, but the typically small g-factors of semiconductors limit its effectiveness. Magnetic proximity effects offer an alternative by introducing valley asymmetry [1,10,11]. Valley phenomena in AMs have recently

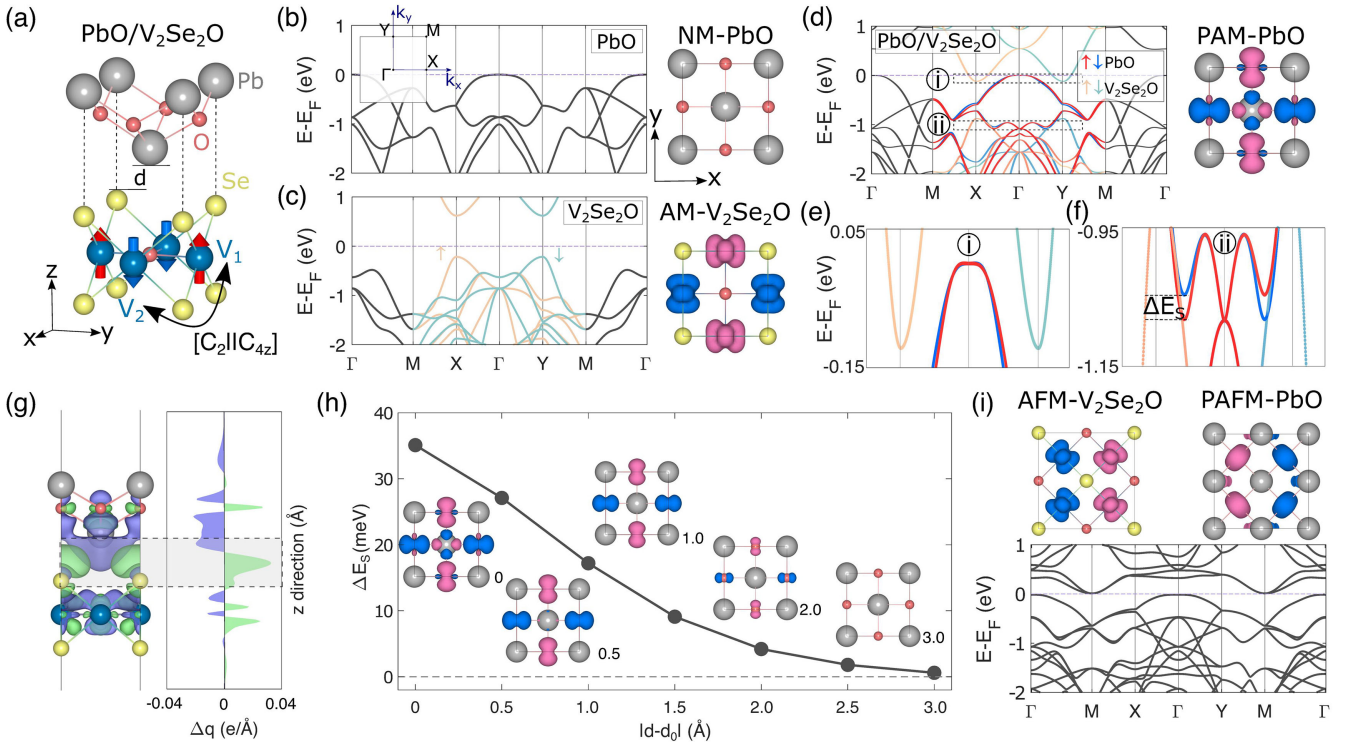

FIG. 2. (a) Crystal structure of PbO/V_2Se_2O heterostructure. The spin sublattices of V_2Se_2O are connected by $[C_2\|C_{4z}]$ symmetry. (b)–(d) Calculated bands and spin densities of pristine monolayers PbO and V_2Se_2O, and their heterostructure. The inset in (b) shows the first Brillouin zone. (e),(f) Enlarged views of the regions labeled "(i)" and "(ii)" in (d). (g) Differential charge density of the PbO/V_2Se_2O heterostructure and its planar average, $\Delta q(z)$. Green (purple) indicates charge accumulation (depletion) and the isosurface value is 5×10^{-4} e/bohr^3. (h) Spin splitting ΔE_S in (f) with the spin densities, as a function of the interlayer distance d in (a), where d_0 is the equilibrium value. (i) Same as (d) but for a proximitized AFM PbO (PAFM-PbO), realized when PbO is placed on a $\sqrt{2} \times \sqrt{2}$ V_2Se_2O supercell in a conventional AFM state. For all bands, black denotes spin-degenerate states; red and blue indicate spin-up and spin-down bands of the PAM component (PbO), while yellow and green represent the corresponding bands of the V_2Se_2O component.

attracted growing attention [26,87–89]. In particular, monolayer V_2Se_2O has been predicted to host a unique symmetry-paired spin-valley locking that links spin and valley space with real space, enabling giant piezomagnetism and large noncollinear spin currents [26].

Motivated by this, we explore whether such valley physics can be transferred into an NM material through the AMPE, using a PbS/V_2Se_2O heterostructure as an example [Fig. 3(a)]. Monolayer PbS, known for its rich topological, valleytronic, and optoelectronic properties [90], exhibits spin-valley degeneracy in its pristine state [Fig. 3(b)]. When coupled to V_2Se_2O, PbS inherits the altermagnetic feature of symmetry-paired spin-valley locking through the AMPE, as evidenced by the characteristic spin splitting in Fig. 3(c) and the corresponding rotation-symmetry-linked spin-density patterns shown in Supplemental Material [77]. This pairing enables strain-tunable valley polarization: breaking the mirror symmetry between the X and Y valleys converts them from degenerate to polarized states. Uniaxial strain along x or y shifts their relative energies in opposite directions, producing a controllable valley splitting that grows monotonically under either compressive or tensile strain [Fig. 3(e)]. This effect is substantial even under moderate strain—for example, 3% tensile strain along x yields a 152 meV valence-band splitting [Fig. 3(d), Supplemental Material [77]], far exceeding the thermal energy at 300 K. Such a robust splitting ensures stable valley polarization and enables practical control of valley populations through mechanical or substrate engineering. These results demonstrate that the AMPE provides a general route to induce spin-valley polarization in otherwise nonmagnetic materials. By combining interfacial coupling with strain engineering, one can realize electrically and mechanically tunable valley functionalities, opening new opportunities for spintronic and valleytronic applications in AM-based heterostructures.

Topological superconductivity—Proximity effects provide one of the most promising routes to realize topological superconductivity and host Majorana modes (MM), essential for fault-tolerant quantum computing [91–93]. The conventional platform, an s-wave superconductor proximitized into a semiconductor with strong spin-orbit coupling under an

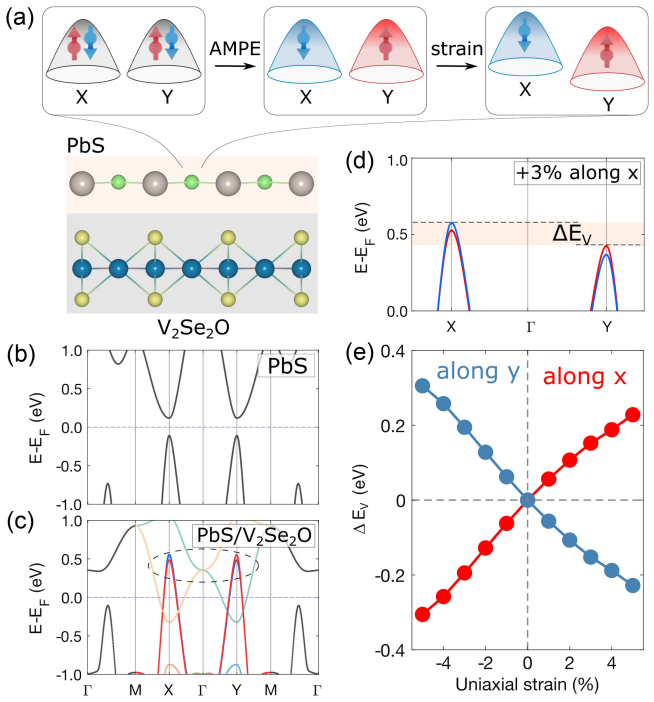

FIG. 3. (a) Schematic of the PbS/V_2Se_2O heterostructure illustrating the AMPE- and strain-induced spin and valley splitting in a monolayer PbS. (b),(c) Calculated bands of the monolayer PbS and PbS/V_2Se_2O heterostructure. (d) Bands of the AM-proximitized monolayer PbS under 3% uniaxial tensile strain along the x axis, showing valley splitting, ΔE_V. (e) Strain-dependent ΔE_V. Band color codes as in Fig. 2.

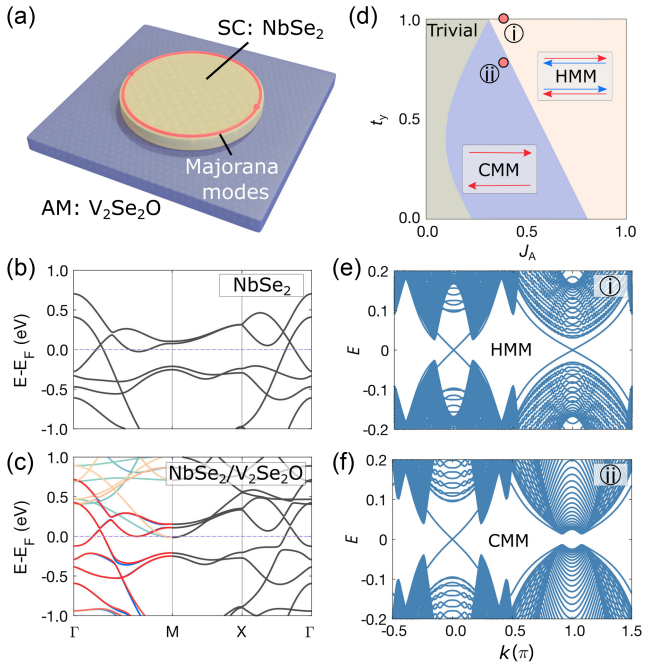

FIG. 4. (a) Schematic transformation of an s-wave superconductor $NbSe_2$ into a topological superconductor hosting edge MM (red circle) via the AMPE from V_2Se_2O. (b),(c) Bands of a $NbSe_2$ supercell, and the $NbSe_2/V_2Se_2O$ heterostructure. (d) Topological phase diagram of the PAM-$NbSe_2$ obtained from Eq. (1). (e),(f) Ribbon spectra of PAM-$NbSe_2$ showing helical and chiral MM (HMM and CMM). Parameters are $t_x = 1$, $\mu = 0.6$, $\lambda_R = 0.2$, $J_A = 0.4$, $\Delta = 0.2$. $t_y = 1$ in (e) and $t_y = 0.8$ in (f). Band color codes as in Fig. 2.

external magnetic field, has yielded multiple signatures of topological superconductivity [92]. However, this approach requires applied magnetic fields that compete with superconductivity. In contrast, the AMPE offers a distinct advantage: it induces momentum-dependent spin splitting without net magnetization or external fields, thus preserving the superconducting gap while enabling new routes to engineer topological superconducting states [64–66].

To explore this possibility, we consider a platform composed of the well-studied vdW s-wave superconductor $NbSe_2$ placed on V_2Se_2O [Fig. 4(a)]. In this configuration, the AMPE-induced splitting from V_2Se_2O is expected to modify the pairing of $NbSe_2$ and can drive it into a topological superconductor hosting edge MM. Our first-principles calculations confirm that pristine $NbSe_2$ exhibits spin-degenerate bands [Fig. 4(b)], while in the $NbSe_2/V_2Se_2O$ heterostructure these bands acquire altermagnetic spin splitting as seen in Fig. 4(c) and Supplemental Material [77], demonstrating that the AMPE penetrates the superconducting layer without introducing net magnetization.

To analyze the superconducting properties of proximitized $NbSe_2$, we construct an effective model in the Nambu basis,

$$\begin{aligned} H_{\mathrm{BdG}} = {} & (t_x \cos k_x + t_y \cos k_y - \mu)\sigma_0\tau_z \\ & + \lambda_R(\sin k_y \sigma_x\tau_z - \sin k_x \sigma_y\tau_z) \\ & + J_A(\cos k_x - \cos k_y)\sigma_z\tau_0 + \Delta\sigma_0\tau_x, \end{aligned} \tag{1}$$

where $\sigma_i(\tau_i)$ are Pauli matrices in spin (particle-hole) space. The model includes kinetic hopping terms $t_{x/y}$, chemical potential μ, s-wave pairing Δ, the AMPE strength J_A, and the Rashba spin-orbit coupling strength λ_R, which arises from broken out-of-plane mirror symmetry at the interface and is essential for driving $NbSe_2$ into a topological superconducting phase [94,95], as detailed in Supplemental Material [77].

From gap-closing conditions and the calculated topological invariants [77,96], we obtain the phase diagram in Fig. 4(d). For isotropic hopping ($t_x = t_y$), crystalline symmetry enforces a valley degeneracy that, with suitable J_A, yields a helical topological superconductor hosting pairs of helical MMs at the edges [Fig. 4(e)]. Breaking this crystalline relation ($t_x \neq t_y$) lifts the valley degeneracy, allowing valley-selective topological transitions: one valley becomes topological while the other remains trivial. The edge spectrum then contains a single chiral MM per

boundary [Fig. 4(f)]. This symmetry-controlled switch between helical and chiral MMs within a single platform is a key advantage of AMPE-based designs. Because altermagnetism can be flexibly tuned by various dynamic means [31,32,97], the AMPE enables controllable manipulation of MMs, offering unprecedented opportunities for their fusion and braiding [98–100] central to topological quantum computing.

Beyond the V_2Se_2O-based heterostructures, we further demonstrate that the AMPE is a generic interfacial mechanism by realizing it in heterostructures between other nonmagnetic layers and diverse altermagnetic platforms, including V_2Se_2O derivatives, Ruddlesden-Popper perovskites (e.g., $Ca_3Mn_2O_7$ [49]), and the experimentally established metallic altermagnet CrSb [34], as detailed in Supplemental Material [77]. These results further reinforce both the generality and experimental feasibility of the AMPE.

Our proposed AMPE shifts the role of AMs from intrinsic or bulk mechanisms to an interfacial route. This conceptual advance significantly broadens their scope, enabling their momentum-alternating spin textures to be harnessed in otherwise NM systems. Just as ferromagnetic proximity can induce energy splittings beyond those achievable with external fields [1], the AMPE offers comparable advantages while avoiding stray fields and net magnetization. This field-free distinction is especially crucial for proximity-induced topological superconductivity, where conventional Zeeman-based schemes are often limited to semiconductors with large g-factors even under magnetic textures and fringing fields [100,101].

More broadly, the tunable spin and symmetry properties of altermagnets make the AMPE a versatile platform for realizing emergent states that would otherwise demand complex materials or multiple proximity effects [1]. A natural outlook is to identify the governing factors and control knobs of the AMPE strength, as well as the characteristic energy and timescales for reconfiguring altermagnetic order. Such efforts will be essential for assessing the feasibility of dynamical control over spin-dependent and topological responses [14,95], opening new opportunities to manipulate quantum phases in both normal and superconducting states.

Acknowledgments—We thank Yuntian Liu for helpful discussions. T. Z. acknowledges support from Hui Yang and inspiration from Avery Zhou and Mila Zhou. This work is supported by the Zhejiang Provincial Natural Science Foundation of China (LR25A040001), the Zhejiang Provincial Leading Innovative and Entrepreneurial Team Project (2025R01017), the National Natural Science Foundation of China (12474155, 12504108, and 11904250), the Zhejiang Pioneer Project under Grant No. 2025C06SA201986, the China Postdoctoral Science Foundation (2025M773440), the U.S. DOE, Office of Science BES, Award No. DE-SC0004890 (I. Ž. for AMs), and the U.S. ONR under Award No. MURI N000142212764 (I. Ž. for MMs).

Z. Z. and R. H. contributed equally to this work.

Data availability—The data that support the findings of this letter are openly available [102].

[1] I. Žutić, A. Matos-Abiague, B. Scharf, H. Dery, and K. Belashchenko, Proximitized materials, Mater. Today **22**, 85 (2019).
[2] A. I. Buzdin, Proximity effects in superconductor-ferromagnet heterostructures, Rev. Mod. Phys. **77**, 935 (2005).
[3] J. J. Hauser, Magnetic proximity effect, Phys. Rev. **187**, 580 (1969).
[4] P. Manna and S. Yusuf, Two interface effects: Exchange bias and magnetic proximity, Phys. Rep. **535**, 61 (2014).
[5] M. Gmitra and J. Fabian, Graphene on transition-metal dichalcogenides: A platform for proximity spin-orbit physics and optospintronics, Phys. Rev. B **92**, 155403 (2015).
[6] Z. Wang, C. Tang, R. Sachs, Y. Barlas, and J. Shi, Proximity-induced ferromagnetism in graphene revealed by the anomalous Hall effect, Phys. Rev. Lett. **114**, 016603 (2015).
[7] C. Zhao, T. Norden, P. Zhang, P. Zhao, Y. Cheng, F. Sun, J. P. Parry, P. Taheri, J. Wang, Y. Yang, T. Scrace, K. Kang, S. Yang, G.-X. Miao, R. Sabirianov, G. Kioseoglou, W. Huang, A. Petrou, and H. Zeng, Enhanced valley splitting in monolayer WSe_2 due to magnetic exchange field, Nat. Nanotechnol. **12**, 757 (2017).
[8] B. Scharf, G. Xu, A. Matos-Abiague, and I. Žutić, Magnetic proximity effects in transition-metal dichalcogenides: Converting excitons, Phys. Rev. Lett. **119**, 127403 (2017).
[9] D. Zhong, K. L. Seyler, X. Linpeng, N. P. Wilson, T. Taniguchi, K. Watanabe, M. A. McGuire, K.-M. C. Fu, D. Xiao, W. Yao, and X. Xu, Layer-resolved magnetic proximity effect in van der Waals heterostructures, Nat. Nanotechnol. **15**, 187 (2020).
[10] J. Choi, C. Lane, J.-X. Zhu, and S. A. Crooker, Asymmetric magnetic proximity interactions in $MoSe_2/CrBr_3$ van der Waals heterostructures, Nat. Mater. **22**, 305 (2023).
[11] T. Zhou and I. Žutić, Asymmetry in the magnetic neighbourhood, Nat. Mater. **22**, 284 (2023).
[12] V. Baltz, A. Manchon, M. Tsoi, T. Moriyama, T. Ono, and Y. Tserkovnyak, Antiferromagnetic spintronics, Rev. Mod. Phys. **90**, 015005 (2018).
[13] D. Shao and E. Tsymbal, Antiferromagnetic tunnel junctions for spintronics, npj Spintron. **2**, 13 (2024).
[14] I. Žutić, J. Fabian, and S. Das Sarma, Spintronics: Fundamentals and applications, Rev. Mod. Phys. **76**, 323 (2004).
[15] J. R. Schaibley, H. Yu, G. Clark, P. Rivera, J. S. Ross, K. L. Seyler, W. Yao, and X. Xu, Valleytronics in 2D materials, Nat. Rev. Mater. **1**, 16055 (2016).

[16] K. L. Seyler *et al.*, Valleytronics in 2D Materials Roadmap, arXiv:2603.01427.

[17] Z. Qiao, W. Ren, H. Chen, L. Bellaiche, Z. Zhang, A. H. MacDonald, and Q. Niu, Quantum anomalous Hall effect in graphene proximity coupled to an antiferromagnetic insulator, Phys. Rev. Lett. **112**, 116404 (2014).

[18] R. Cai, I. Žutić, and W. Han, Superconductor/ferromagnet heterostructures: A platform for superconducting spintronics and quantum computation, Adv. Quantum Technol. **6**, 2200080 (2023).

[19] L. Fu and C. L. Kane, Superconducting proximity effect and Majorana fermions at the surface of a topological insulator, Phys. Rev. Lett. **100**, 096407 (2008).

[20] C. Wu, K. Sun, E. Fradkin, and S.-C. Zhang, Fermi liquid instabilities in the spin channel, Phys. Rev. B **75**, 115103 (2007).

[21] S. Hayami, Y. Yanagi, and H. Kusunose, Momentum-dependent spin splitting by collinear antiferromagnetic ordering, J. Phys. Soc. Jpn. **88**, 123702 (2019).

[22] L. D. Yuan, Z. Wang, J. W. Luo, E. I. Rashba, and A. Zunger, Giant momentum-dependent spin splitting in centrosymmetric low-Z antiferromagnets, Phys. Rev. B **102**, 014422 (2020).

[23] L. Šmejkal, R. González-Hernández, T. Jungwirth, and J. Sinova, Crystal time-reversal symmetry breaking and spontaneous Hall effect in collinear antiferromagnets, Sci. Adv. **6**, eaaz8809 (2020).

[24] I. I. Mazin, K. Koepernik, M. D. Johannes, R. González-Hernández, and L. Šmejkal, Prediction of unconventional magnetism in doped $FeSb_2$, Proc. Natl. Acad. Sci. U.S.A. **118**, e2108924118 (2021).

[25] L. D. Yuan, Z. Wang, J. W. Luo, and A. Zunger, Prediction of low-Z collinear and noncollinear antiferromagnetic compounds having momentum-dependent spin splitting even without spin-orbit coupling, Phys. Rev. Mater. **5**, 014409 (2021).

[26] H. Ma, M. Hu, N. Li, J. Liu, W. Yao, J. Jia, and J. Liu, Multifunctional antiferromagnetic materials with giant piezomagnetism and noncollinear spin current, Nat. Commun. **12**, 2846 (2021).

[27] Y.-P. Zhu *et al.*, Observation of plaid-like spin splitting in a noncoplanar antiferromagnet, Nature (London) **626**, 523 (2024).

[28] Q. Liu, X. Dai, and S. Blügel, Different facets of unconventional magnetism, Nat. Phys. **21**, 329 (2025).

[29] L. Šmejkal, J. Sinova, and T. Jungwirth, Beyond conventional ferromagnetism and antiferromagnetism: A phase with nonrelativistic spin and crystal rotation symmetry, Phys. Rev. X **12**, 031042 (2022).

[30] L. Šmejkal, J. Sinova, and T. Jungwirth, Emerging research landscape of altermagnetism, Phys. Rev. X **12**, 040501 (2022).

[31] L. Bai, W. Feng, S. Liu, L. Šmejkal, Y. Mokrousov, and Y. Yao, Altermagnetism: Exploring new frontiers in magnetism and spintronics, Adv. Funct. Mater. **34**, 2409327 (2024).

[32] C. Song, H. Bai, Z. Zhou, L. Han, H. Reichlova, J. H. Dil, J. Liu, X. Chen, and F. Pan, Altermagnets as a new class of functional materials, Nat. Rev. Mater. **10**, 473 (2025).

[33] J. Krempaský *et al.*, Altermagnetic lifting of Kramers spin degeneracy, Nature (London) **626**, 517 (2024).

[34] Z. Zhou, X. Cheng, M. Hu, R. Chu, H. Bai, L. Han, J. Liu, F. Pan, and C. Song, Manipulation of the altermagnetic order in CrSb via crystal symmetry, Nature (London) **638**, 645 (2025).

[35] F. Zhang, X. Cheng, Z. Yin, C. Liu, L. Deng, Y. Qiao, Z. Shi, S. Zhang, J. Lin, Z. Liu, M. Ye, Y. Huang, X. Meng, C. Zhang, T. Okuda, K. Shimada, S. Cui, Y. Zhao, G.-H. Cao, S. Qiao, J. Liu, and C. Chen, Crystal-symmetry-paired spin-valley locking in a layered room-temperature metallic altermagnet candidate, Nat. Phys. **21**, 760 (2025).

[36] B. Jiang *et al.*, A metallic room-temperature d-wave altermagnet, Nat. Phys. **21**, 754 (2025).

[37] S. Sheoran and P. Dev, Spontaneous anomalous Hall effect in two-dimensional altermagnets, Phys. Rev. B **111**, 184407 (2025).

[38] R. Chen, Z.-M. Wang, K. Wu, H.-P. Sun, B. Zhou, R. Wang, and D.-H. Xu, Probing *k*-space alternating spin polarization via the anomalous Hall effect, Phys. Rev. Lett. **135**, 096602 (2025).

[39] S. Bhowal and A. Bose, Non-relativistic spin splitting: Features and functionalities, arXiv:2510.20306.

[40] J. D. Cao, K. S. Denisov, Y. Liu, and I. Žutić, Symmetry classification for alternating excitons in two-dimensional altermagnets, Phys. Rev. Lett. **135**, 266703 (2025).

[41] T. Jungwirth, J. Sinova, P. Wadley, D. Kriegner, H. Reichlova, F. Krizek, H. Ohno, and L. Šmejkal, Altermagnetic spintronics, arXiv:2508.09748.

[42] D.-F. Shao, S.-H. Zhang, M. Li, C.-B. Eom, and E. Y. Tsymbal, Spin-neutral currents for spintronics, Nat. Commun. **12**, 7061 (2021).

[43] R. Takagi, R. Hirakida, Y. Settai, R. Oiwa, H. Takagi, A. Kitaori, K. Yamauchi, H. Inoue, J.-i. Yamaura, D. Nishio-Hamane, S. Itoh, S. Aji, H. Saito, T. Nakajima, T. Nomoto, R. Arita, and S. Seki, Spontaneous Hall effect induced by collinear antiferromagnetic order at room temperature, Nat. Mater. **24**, 63 (2025).

[44] X. Chen, Y. Liu, P. Liu, Y. Yu, J. Ren, J. Li, A. Zhang, and Q. Liu, Unconventional magnons in collinear magnets dictated by spin space groups, Nature (London) **640**, 349 (2025).

[45] L.-S. Liu, K. Shao, H.-D. Li, X. Wan, W. Chen, and D. Y. Xing, Altermagnetic spin precession and spin transistor, Phys. Rev. Lett. **136**, 106301 (2026).

[46] X. Duan, J. Zhang, Z. Zhu, Y. Liu, Z. Zhang, I. Žutić, and T. Zhou, Antiferroelectric altermagnets: Antiferroelectricity alters magnets, Phys. Rev. Lett. **134**, 106801 (2025).

[47] Z. Zhu, X. Duan, J. Zhang, B. Hao, I. Žutić, and T. Zhou, Two-dimensional ferroelectric altermagnets: From model to material realization, Nano Lett. **25**, 9456 (2025).

[48] Z. Zhu, Y. Liu, X. Duan, J. Zhang, B. Hao, S.-H. Wei, I. Žutić, and T. Zhou, Emergent multiferroic altermagnets and spin control via noncollinear molecular polarization, Sci. China Phys. Mech. Astron. **68**, 127562 (2025).

[49] M. Gu, Y. Liu, H. Zhu, K. Yananose, X. Chen, Y. Hu, A. Stroppa, and Q. Liu, Ferroelectric switchable altermagnetism, Phys. Rev. Lett. **134**, 106802 (2025).

[50] W. Sun, C. Yang, W. Wang, Y. Liu, X. Wang, S. Huang, and Z. Cheng, Proposing altermagnetic-ferroelectric type-III multiferroics with robust magnetoelectric coupling, Adv. Mater. **37**, 2502575 (2025).

[51] R. Cao, R. Dong, R. Fei, and Y. Yao, Designing spin-driven multiferroics in altermagnets, arXiv:2412.20347.
[52] W.-T. Guo, J. Xu, Y. Yang, H. Wang, and H. Zhang, Altermagnetic type-II multiferroics with Néel-order-locked electric polarization, arXiv:2505.01964.
[53] A. Urru, D. Seleznev, Y. Teng, S. Y. Park, S. E. Reyes-Lillo, and K. M. Rabe, G-type antiferromagnetic $BiFeO_3$ is a multiferroic g-wave altermagnet, Phys. Rev. B **112**, 104411 (2025).
[54] R. Peng, S. Fang, P. Ho, F. Liu, T. Zhou, J. Liu, and Y. S. Ang, Ferroelastic altermagnetism, npj Quantum Mater. **11**, 5 (2026).
[55] Z. Cui, Z. Zhu, X. Duan, B. Hao, X. Chen, J. Zhang, and T. Zhou, Symmetry-driven unconventional magnetoelectric coupling in perovskite altermagnets: From bulk to the two-dimensional limit, arXiv:2601.05602.
[56] Z. Zhu, X. Chen, X. Duan, Z. Cui, J. Zhang, I. Žutić, and T. Zhou, Altermagnetoelectric spin field effect transistor, arXiv:2512.02974.
[57] H.-Y. Ma and J.-F. Jia, Altermagnetic topological insulator and the selection rules, Phys. Rev. B **110**, 064426 (2024).
[58] P.-J. Guo, Z.-X. Liu, and Z.-Y. Lu, Quantum anomalous Hall effect in collinear antiferromagnetism, npj Comput. Mater. **9**, 70 (2023).
[59] P. Feng, C.-Y. Tan, M. Gao, X.-W. Yan, Z.-X. Liu, P.-J. Guo, F. Ma, and Z.-Y. Lu, Type-II quantum spin Hall insulator, arXiv:2503.13397.
[60] R.-W. Zhang, C. Cui, Y. Wang, J. Duan, Z.-M. Yu, and Y. Yao, Quantized spin-Hall conductivity in altermagnet Fe_2Te_2O with mirror-spin coupling, arXiv:2503.10681.
[61] J. Nag, B. Das, S. Bhowal, Y. Nishioka, B. Bandyopadhyay, S. Sarker, S. Kumar, K. Kuroda, V. Gopalan, A. Kimura, K. G. Suresh, and A. Alam, GdAlSi: An antiferromagnetic topological Weyl semimetal with nonrelativistic spin splitting, Phys. Rev. B **110**, 224436 (2024).
[62] X. Chen, J. Zhang, B. Hao, J. Qian, Z. Zhu, I. Žutić, Z. Zhang, and T. Zhou, Altermagnets enable gate-switchable helical and chiral topological transport with spin-valley-momentum-locked dual protection, arXiv:2603.06487.
[63] B. Brekke, A. Brataas, and A. Sudbø, Two-dimensional altermagnets: Superconductivity in a minimal microscopic model, Phys. Rev. B **108**, 224421 (2023).
[64] Y.-X. Li and C.-C. Liu, Majorana corner modes and tunable patterns in an altermagnet heterostructure, Phys. Rev. B **108**, 205410 (2023).
[65] D. Zhu, Z.-Y. Zhuang, Z. Wu, and Z. Yan, Topological superconductivity in two-dimensional altermagnetic metals, Phys. Rev. B **108**, 184505 (2023).
[66] S. A. A. Ghorashi, T. L. Hughes, and J. Cano, Altermagnetic routes to Majorana modes in zero net magnetization, Phys. Rev. Lett. **133**, 106601 (2024).
[67] J. A. Ouassou, A. Brataas, and J. Linder, dc Josephson effect in altermagnets, Phys. Rev. Lett. **131**, 076003 (2023).
[68] S.-B. Zhang, L.-H. Hu, and T. Neupert, Finite-momentum cooper pairing in proximitized altermagnets, Nat. Commun. **15**, 1801 (2024).
[69] P. Lazić, K. D. Belashchenko, and I. Žutić, Effective gating and tunable magnetic proximity effects in two-dimensional heterostructures, Phys. Rev. B **93**, 241401(R) (2016).
[70] J. Xu, S. Singh, J. Katoch, G. Wu, T. Zhu, I. Žutić, and R. K. Kawakami, Spin inversion in graphene spin valves by gate-tunable magnetic proximity effect at one-dimensional contacts, Nat. Commun. **9**, 2869 (2018).
[71] P. E. Faria Junior, T. Naimer, K. M. McCreary, B. T. Jonker, J. J. Finley, S. A. Crooker, J. Fabian, and A. V. Stier, Proximity-enhanced valley Zeeman splitting at the WS_2/graphene interface, 2D Mater. **10**, 034002 (2023).
[72] K. Zollner, P. E. Faria Junior, and J. Fabian, Strong manipulation of the valley splitting upon twisting and gating in $MoSe_2/CrI_3$ and WSe_2/CrI_3 van der Waals heterostructures, Phys. Rev. B **107**, 035112 (2023).
[73] K. Huang, E. Schwartz, D.-F. Shao, A. A. Kovalev, and E. Y. Tsymbal, Magnetic antiskyrmions in two-dimensional van der Waals magnets engineered by layer stacking, Phys. Rev. B **109**, 024426 (2024).
[74] H. Lin, J. Si, X. Zhu, K. Cai, H. Li, L. Kong, X. Yu, and H.-H. Wen, Structure and physical properties of $CsV_2Se_{2-x}O$ and V_2Se_2O, Phys. Rev. B **98**, 075132 (2018).
[75] S. Barraza-Lopez, B. M. Fregoso, J. W. Villanova, Stuart S. P. Parkin, and K. Chang, Colloquium: Physical properties of group-IV monochalcogenide monolayers, Rev. Mod. Phys. **93**, 011001 (2021).
[76] P. Kumar, J. Liu, P. Ranjan, Y. Hu, S. S. Yamijala, S. K. Pati, J. Irudayaraj, and G. J. Cheng, Alpha lead oxide (α-PbO): A new 2D material with visible light sensitivity, Small **14**, 1703346 (2018).
[77] See Supplemental Material at http://link.aps.org/supplemental/10.1103/kqy8-myz1 for the discussion of the first-principles calculation methods, symmetry analysis of the AMPE, AMPE-induced topological superconductivity, additional AMPE material platforms, and the influence of strain, charge transfer, and antiferromagnetic configurations, which includes Refs. [78–82].
[78] G. Kresse and J. Furthmüller, Efficient iterative schemes for *ab initio* total-energy calculations using a plane-wave basis set, Phys. Rev. B **54**, 11169 (1996).
[79] S. Grimme, Semiempirical GGA-type density functional constructed with a long-range dispersion correction, J. Comput. Chem. **27**, 1787 (2006).
[80] R. Xu, Y. Gao, and J. Liu, Chemical design of monolayer altermagnets, Natl. Sci. Rev. **13**, nwaf528 (2025).
[81] X. Xu and L. Yang, Alterpiezoresponse in two-dimensional Lieb-lattice altermagnets, Nano Lett. **25**, 11870 (2025).
[82] L. Fu and C. L. Kane, Topological insulators with inversion symmetry, Phys. Rev. B **76**, 045302 (2007).
[83] D. Xiao, W. Yao, and Q. Niu, Valley-contrasting physics in graphene: Magnetic moment and topological transport, Phys. Rev. Lett. **99**, 236809 (2007).
[84] T. Zhou, S. Cheng, M. Schleenvoigt, P. Schüffelgen, H. Jiang, Z. Yang, and I. Žutić, Quantum spin-valley Hall kink states: From concept to materials design, Phys. Rev. Lett. **127**, 116402 (2021).
[85] T. Zhou, J. Zhang, B. Zhao, H. Zhang, and Z. Yang, Quantum spin-quantum anomalous Hall insulators and topological transitions in functionalized Sb(111) monolayers, Nano Lett. **15**, 5149 (2015).
[86] T. Zhou, J. Zhang, H. Jiang, I. Žutić, and Z. Yang, Giant spin-valley polarization and multiple Hall effect in

functionalized bismuth monolayers, npj Quantum Mater. **3**, 39 (2018).

[87] R.-W. Zhang, C. Cui, R. Li, J. Duan, L. Li, Z.-M. Yu, and Y. Yao, Predictable gate-field control of spin in altermagnets with spin-layer coupling, Phys. Rev. Lett. **133**, 056401 (2024).

[88] Y.-Q. Li, Y.-K. Zhang, X.-L. Lu, Y.-P. Shao, Z.-Q. Bao, J.-D. Zheng, W.-Y. Tong, and C.-G. Duan, Ferrovalley physics in stacked bilayer altermagnetic systems, Nano Lett. **25**, 6032 (2025).

[89] S.-D. Guo, Y. Liu, J. Yu, and C.-C. Liu, Valley polarization in twisted altermagnetism, Phys. Rev. B **110**, L220402 (2024).

[90] W. Wan, Y. Yao, L. Sun, C.-C. Liu, and F. Zhang, Topological, valleytronic, and optical properties of monolayer PbS, Adv. Mater. **29**, 1604788 (2017).

[91] K. Flensberg, F. von Oppen, and A. Stern, Engineered platforms for topological superconductivity and Majorana zero modes, Nat. Rev. Mater. **6**, 944 (2021).

[92] S. Das Sarma, M. Freedman, and C. Nayak, Majorana zero modes and topological quantum computation, npj Quantum Inf. **1**, 15001 (2015).

[93] U. Güngördü and A. A. Kovalev, Majorana bound states with chiral magnetic textures, J. Appl. Phys. **132**, 041101 (2022).

[94] H. Yi, L.-H. Hu, Y. Wang, R. Xiao, J. Cai, D. R. Hickey, C. Dong, Y.-F. Zhao, L.-J. Zhou, R. Zhang *et al.*, Crossover from Ising- to Rashba-type superconductivity in epitaxial Bi_2Se_3/monolayer $NbSe_2$ heterostructures, Nat. Mater. **21**, 1366 (2022).

[95] M. Amundsen, J. Linder, J. W. A. Robinson, I. Žutić, and N. Banerjee, Colloquium: Spin-orbit effects in superconducting hybrid structures, Rev. Mod. Phys. **96**, 021003 (2024).

[96] D. Zhu, D. Liu, Z.-Y. Zhuang, Z. Wu, and Z. Yan, Field-sensitive dislocation bound states in two-dimensional *d*-wave altermagnets, Phys. Rev. B **110**, 165141 (2024).

[97] Y. Chen, X. Liu, H.-Z. Lu, and X. C. Xie, Electrical switching of altermagnetism, Phys. Rev. Lett. **135**, 016701 (2025).

[98] T. Zhou, M. C. Dartiailh, K. Sardashti, J. E. Han, A. Matos-Abiague, J. Shabani, and I. Žutić, Fusion of Majorana bound states with mini-gate control in two-dimensional systems, Nat. Commun. **13**, 1738 (2022).

[99] T. Zhou, M. C. Dartiailh, W. Mayer, J. E. Han, A. Matos-Abiague, J. Shabani, and I. Žutić, Phase control of Majorana bound states in a topological X junction, Phys. Rev. Lett. **124**, 137001 (2020).

[100] G. L. Fatin, A. Matos-Abiague, B. Scharf, and I. Žutić, Wireless Majorana bound states: From magnetic tunability to braiding, Phys. Rev. Lett. **117**, 077002 (2016).

[101] T. Zhou, N. Mohanta, J. E. Han, A. Matos-Abiague, and I. Žutić, Tunable magnetic textures in spin valves: From spintronics to Majorana bound states, Phys. Rev. B **99**, 134505 (2019).

[102] Z. Zhu, R. Huang, X. Chen, Z. Cui, X. Duan, J. Zhang, I. Žutić, and T. Zhou, Dataset for "Altermagnetic proximity effect", 10.5281/zenodo.18985478.

Supplemental Material

Altermagnetic Proximity Effect

Ziye Zhu,[1] Richang Huang,[1] Xianzhang Chen,[1] Zhou Cui,[1] Xunkai Duan,[1] Jiayong Zhang,[1,2] Igor Žutić,[3] and Tong Zhou[1,*]

[1]*Eastern Institute for Advanced Study, Eastern Institute of Technology, Ningbo, Zhejiang 315200, China*
[2]*School of Physical Science and Technology, Suzhou University of Science and Technology, Suzhou, 215009, China*
[3]*Department of Physics, University at Buffalo, State University of New York, Buffalo, New York 14260, USA*

SECTION I: FIRST-PRINCIPLES CALCULATION METHODS

The density functional theory (DFT) calculations are carried out within the generalized gradient approximation using the Perdew-Burke-Ernzerhof exchange correlation potential (PBE) as implemented in the Vienna ab initio simulation package (VASP) [1]. We have set the kinetic energy cutoff at 600 eV and the Brillouin zone is sampled by a $9 \times 9 \times 1$ Γ-centered Monkhorst-Pack mesh. The convergence criterion for energy was set to 10^{-6} eV, and the geometry relaxations of the structural models were carried out until the residual force on each atom was less than 10^{-3} eVÅ^{-1}. Van der Waals forces were taken into account by using Grimme's semiempirical correction method [2]. To avoid interactions between neighboring slabs, we include 20 Å of empty space in the z axis. We used Hubbard $U = 5.1$ eV and the Hund's rule coupling $J = 0.8$ eV to treat the strong correlations of the V $3d$ orbitals in V_2Se_2O [3].

Since in Fig. 1 of the main text, we used the PbO/V_2Se_2O heterostructure to demonstrate the AMPE, we considered various stacking configurations of PbO relative to V_2Se_2O to establish the robustness of the chosen structure. Figure S1 shows the variation of the total energy differences as a function of rigid in-plane displacements between the PbO and V_2Se_2O slabs along the x and y axes ([100] and [010] directions). These calculations allow us to determine the ground-state structure of the heterostructure (Stack I), which is subsequently used in all of our calculations.

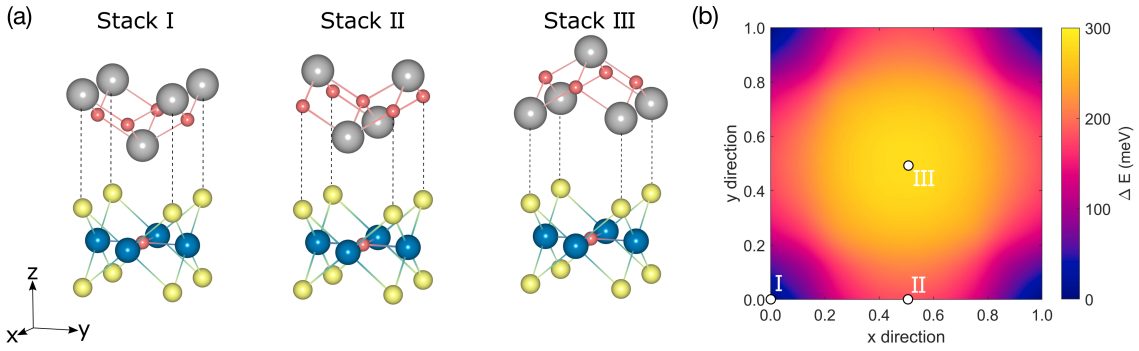

Fig. S1. **(a)** DFT relaxed atomistic structural models of the PbO/V_2Se_2O heterostructure for three distinct stacking configurations. **(b)** Variation of the total energy differences (relative to Stack I) as a function of rigid in-plane displacements between PbO and V_2Se_2O slabs along the x and y axes ([100] and [010] directions).

SECTION II: INFLUENCE OF AFM CONFIGURATIONS

Figure S2 shows the spin density and spin-resolved band structure of the PbO/V_2Se_2O heterostructure under various AFM configurations of V_2Se_2O. In the conventional AFM configurations as in Fig. S2 (b) and (c), the sublattices are related by translation or inversion symmetry, which eliminates the alternating spin splitting. As expected, the induced splitting in PbO disappears, while its spin density develops an AFM feature, indicating a conventional AFM proximity effect. This control case further highlights the AMPE of V_2Se_2O.

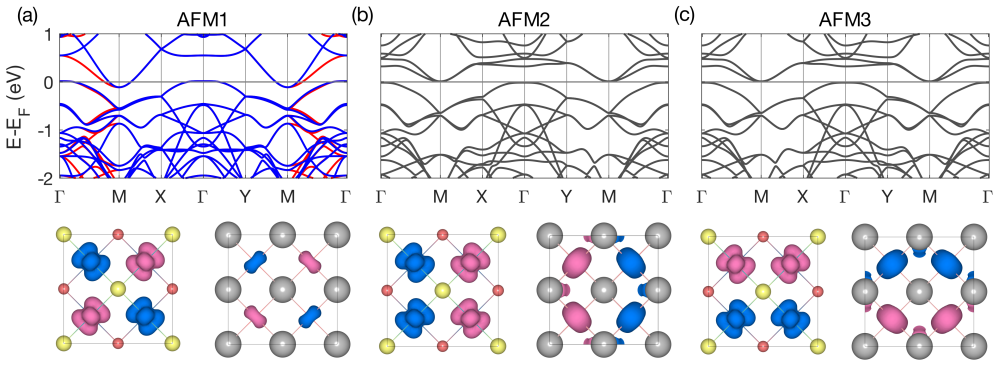

Fig. S2. Band structures and spin charge densities of the PbO/V_2Se_2O heterostructure in a $\sqrt{2} \times \sqrt{2}$ supercell for different antiferromagnetic (AFM) configurations of V_2Se_2O, including **(a)** the altermagnetic state and **(b, c)** conventional AFM states. Black, red, and blue denote the spin degenerate, up, and down bands, respectively.

SECTION III: SYMMETRY ANALYSIS OF AMPE

Within spin-group theory, spin-symmetry operations can be written as $[R_s||R_j]$, where the operation on the left (right) of the double bar acts in spin (real) space. Realizing altermagnetism requires that magnetic sublattices be related by a rotation or mirror operation, rather than by pure translation or inversion.

In Fig. 2 of the main text, we analyze the spin density of PbO, while Fig. S3 extends comparable spin-density visualizations to PbS and $NbSe_2$, respectively. For the PbS/V_2Se_2O heterostructure, both monolayer V_2Se_2O and monolayer PbS crystallize in the P4/mmm space group. Since their symmetries are identical, the spin-symmetry operation for V_2Se_2O in the PbS/V_2Se_2O heterostructure is represented by the $[C_2 \parallel C_{4z}]$ symmetry. The spin density of the PAM-PbS exhibits the same $[C_2 \parallel C_{4z}]$ symmetry, satisfying the symmetry requirements of altermagnetism, as shown in Fig. S3(a). Monolayer $NbSe_2$ belongs to the hexagonal $P\bar{6}m2$ space group. To match the computational setting of V_2Se_2O, we performed a basis transformation on $NbSe_2$, under which its symmetry reduces to the Pm space group, containing only M and t operations. Owing to the different symmetries of $NbSe_2$ and V_2Se_2O in this configuration, the real-space spin density of PAM-$NbSe_2$ exhibits the $[C_2 \parallel M_x]$ symmetry, which also satisfies the symmetry condition for altermagnetism, as illustrated in Fig. S3(b). These results clearly demonstrate the universality of AMPE: the penetrating spin density is reconfigured to satisfy the symmetry requirements of altermagnetism and is not restricted by the specific symmetries of the constituent materials, fully consistent with the nature of a proximity effect.

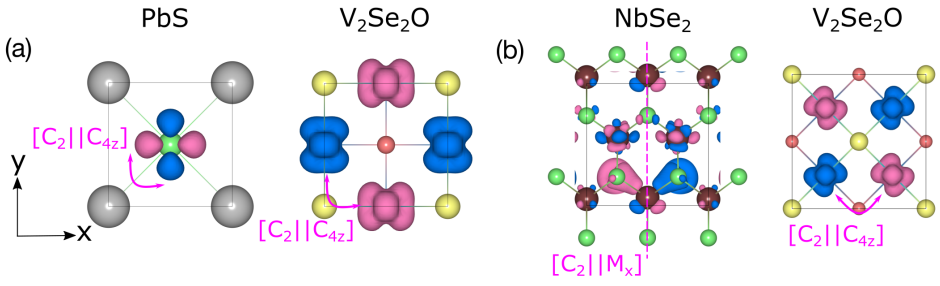

Fig. S3. Calculated spin densities of **(a)** PbS and V_2Se_2O components in PbS/V_2Se_2O heterostructure, and **(b)** $NbSe_2$ and V_2Se_2O components in $NbSe_2$/V_2Se_2O heterostructure.

SECTION IV: INFLUENCE OF CHARGE TRANSFER

In first-principles calculations the two materials are treated within a single periodic cell and must share a common chemical potential, which enforces a single Fermi level for the heterostructure. Depending on the relative band alignment, this common Fermi level (E_F) can intersect bands of one constituent even when interlayer hybridization and charge transfer are weak. To disentangle this "alignment effect" from genuine charge-transfer-induced doping, we performed a control calculation in which we artificially increased the interlayer separation (Fig. S4). At a separation of ~20Å where interlayer coupling and charge transfer are effectively suppressed, the Fermi level still intersects the V_2Se_2O bands. This demonstrates that the appearance of states at E_F in the heterostructure band structure is dominated by the intrinsic band alignment and the enforced common chemical potential in the DFT setup, rather than by significant carrier injection into the magnetic layer.

To directly assess whether any residual interfacial charge redistribution could modify the magnetism, we computed the total energies of the PbO/V_2Se_2O heterostructure for several competing magnetic configurations (Tab. S1). In all cases, the altermagnetic (AM) configuration remains the lowest-energy state, indicating that the magnetic ground state is robust against the small carrier redistribution present in the vdW heterostructure. Consistent with this conclusion, Fig. S4 shows that as the interlayer distance increases (reducing charge transfer), the band alignment and Fermi-level position shift slightly, but the characteristic altermagnetic band features of V_2Se_2O persist throughout. Therefore, any screening or carrier-mediated modifications to the magnetic interactions are not strong enough to change the magnetic ground state in the relevant regime.

To explicitly examine whether such doping could destabilize the altermagnetic order, we evaluated the relative total energies of competing magnetic configurations of V_2Se_2O under electron/hole doping, as summarized in Tab. S2. We find that for doping concentrations up to 0–0.05 electrons/holes per unit cell—well beyond what is typically expected from vdW charge transfer—the altermagnetic (AM) state remains the lowest-energy configuration.

Taken together, these results indicate that the interfacial charge redistribution does not qualitatively change the magnetic ground state of V_2Se_2O in the relevant doping regime, and therefore should not compromise the AMPE-driven superconducting physics.

Table S1. The total energy of various magnetic states for $\sqrt{2} \times \sqrt{2}$ supercell of the PbO/V_2Se_2O heterostructure. The total energy of the corresponding ground state is taken as the reference (0), in units of eV per unit cell.

AM	AFM	FM	NM
0	1.65	0.68	5.27

Table S2. The total energy of various magnetic states for monolayer V_2Se_2O under various electron/hole-doping concentrations (units: electrons/holes per unit cell). For each doping level, the total energy of the corresponding ground state is taken as the reference (0), in units of eV per unit cell.

Electron	AM	AFM	FM	NM	Hole	AM	AFM	FM	NM
0	0	1.13	0.95	5.53	0	0	1.13	0.95	5.52
0.01	0	1.12	0.94	5.52	0.01	0	1.17	0.99	5.56
0.02	0	1.11	0.93	5.51	0.02	0	1.21	1.03	5.59
0.03	0	1.10	0.92	5.51	0.03	0	1.25	1.06	5.63
0.04	0	1.09	0.91	5.50	0.04	0	1.29	1.10	5.66
0.05	0	1.08	0.90	5.49	0.05	0	1.33	1.14	5.70

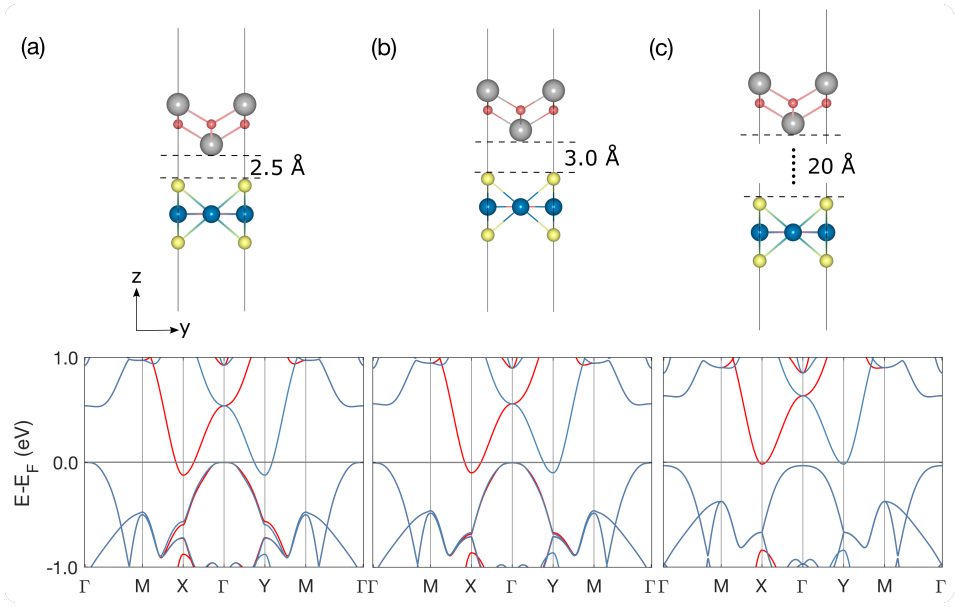

Fig. S4. Schematic structures of the PbO/V_2Se_2O heterostructure with an interlayer distance of **(a)** 2.5 Å (DFT-optimized), an artificially increased distance of **(b)** 3 Å and **(c)** 20 Å, along with their corresponding band structures.

SECTION V: UNIVERSALITY AND EXPERIMENTAL FEASIBILITY OF AMPE

To explicitly demonstrate this universality and experimental feasibility, we have substantially broadened the scope of our study by realizing AMPE in a wider range of heterostructures between nonmagnetic materials and altermagnetic platforms, encompassing van der Waals layered altermagnets (V_2X_2O with X = S/Se/Te; M_2WS_4 with M = Fe/Mn/Co), Ruddlesden-Popper perovskites ($Ca_3Mn_2O_7$ and $Ca_3Fe_2O_7$), and experimentally confirmed metallic altermagnet CrSb, as detailed below.

(i). **V_2X_2O (X = S/Se/Te) and related derivatives:** Fig. S5 presents spin-resolved band structures for heterostructures composed of monolayer altermagnetic V_2X_2O (X = S/Se/Te) combined with various nonmagnetic materials, including monolayer PbO, SnO, and PbS. As highlighted by the dashed ellipses, the nonmagnetic layers clearly develop momentum-dependent spin splitting induced by the AMPE. We emphasize that our analysis is not limited to the specific V_2X_2O compounds shown here. Recent systematic studies [4] have demonstrated that, through symmetry-preserving structural modifications and valence-adaptive chemical substitutions, more than 2600 candidate compounds across four structural frameworks ($M_2A_2B_{1,0}$ and their Janus derivatives) can be designed, among which approximately 670 are predicted to host altermagnetic ground states. We therefore expect that many of these materials will similarly exhibit AMPE when incorporated into heterostructures.

(ii). **M_2WS_4 (M = Fe/Mn/Co):** Ternary transition-metal chalcogenides M_2WS_4 (M = Mn/Fe/Co), characterized by a Lieb lattice, constitute another representative class of van der Waals layered altermagnets [5]. Fig. S6 presents the spin-resolved band structures of the monolayers and their heterostructures formed with various nonmagnetic materials. A pronounced momentum-dependent spin splitting emerges in the nonmagnetic component via the AMPE, thereby driving it into the state of a proximitized altermagnet (PAM).

(iii). **Ruddlesden–Popper perovskites:** Ruddlesden–Popper perovskites constitute an important materials platform for realizing altermagnetism [6]. As a representative example, we consider the widely studied Ruddlesden–Popper perovskite $Ca_3Mn_2O_7$ [7] and demonstrate the AMPE in a heterostructure combining a monolayer $Ca_3Mn_2O_7$ exfoliated from the layered bulk with a nonmagnetic SnO monolayer. The calculated spin-resolved band structures Fig. S7 show that SnO acquires a characteristic altermagnetic spin splitting via proximity to $Ca_3Mn_2O_7$. We further find that this effect persists in the element-substituted counterpart $Ca_3Fe_2O_7$, establishing both the universality and experimental feasibility of AMPE in Ruddlesden–Popper perovskite altermagnets.

(iv). **Experimentally confirmed metallic altermagnets:** Although the altermagnets discussed above are insulating, AMPE is not limited to insulating systems and can also arise in metallic heterostructures, analogous to conventional magnetic proximity effects. To demonstrate this explicitly, we examine the experimentally confirmed metallic altermagnet CrSb [8]. Using graphene as the nonmagnetic layer, we compute the electronic structure of CrSb/graphene heterostructures (Fig. S8). The graphene layer acquires a clear momentum-dependent spin splitting characteristic of altermagnetism, demonstrating that AMPE persists in metallic altermagnetic systems.

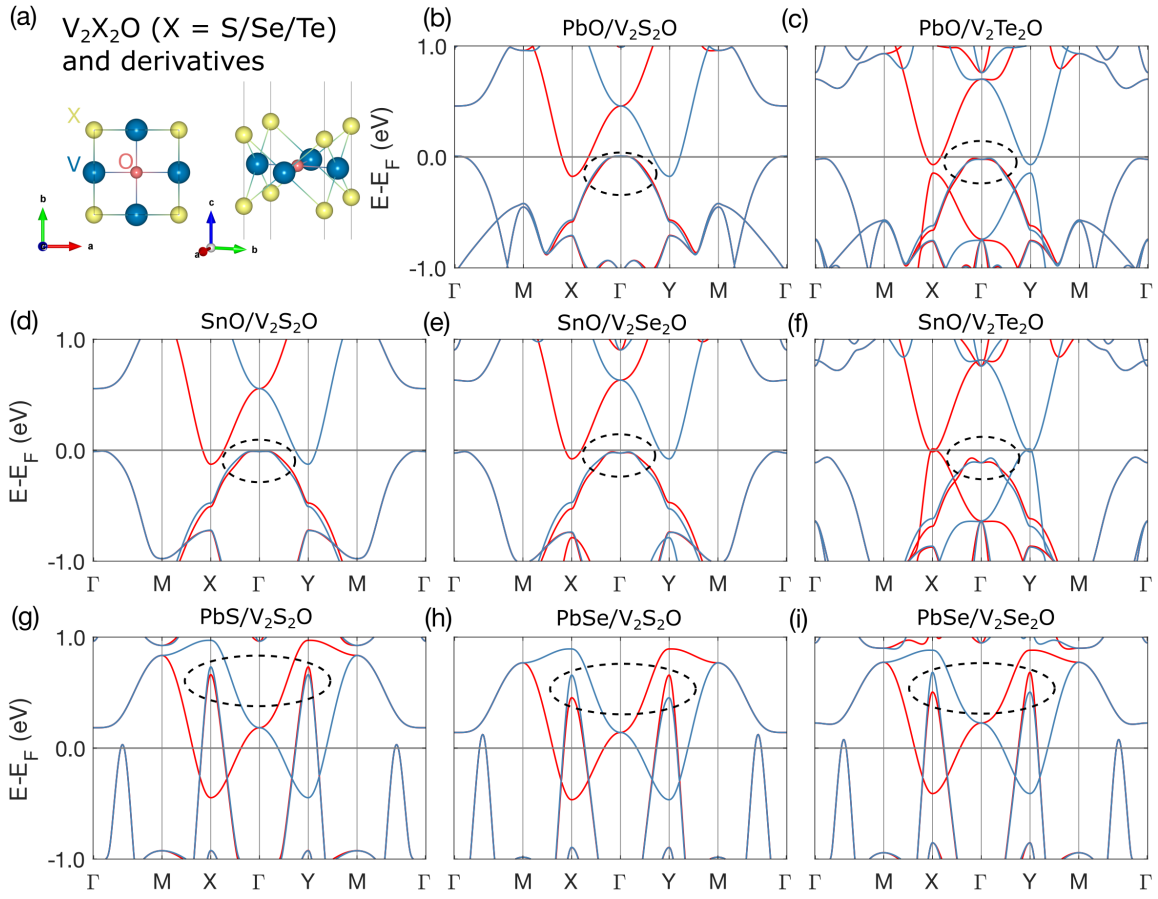

Fig. S5. **(a)** Crystal structure of altermagnetic monolayer V_2X_2O (X = S/Se/Te). **(b)**-**(i)** Calculated spin resolved band structures of the heterostructures formed by V_2X_2O and various nonmagnetic monolayers, including PbO, SnO, and PbSe. The dashed regions highlight proximity-induced altermagnetic spin splitting imprinted on the nonmagnetic layers. Red and blue denote spin-up and spin-down states, respectively.

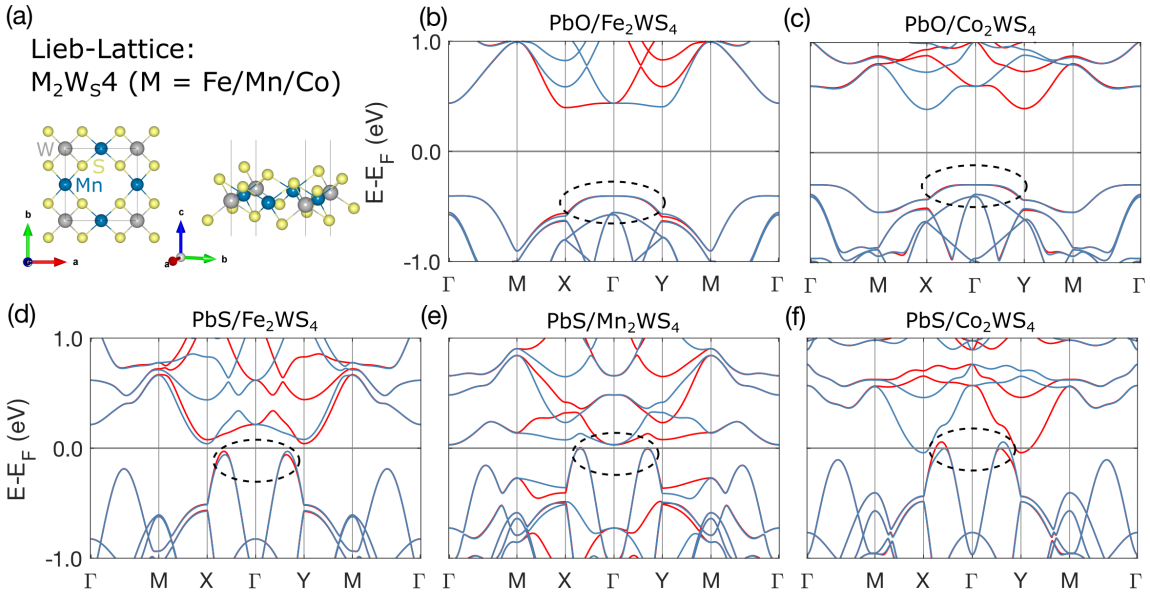

Fig. S6. **(a)** Crystal structure of altermagnetic monolayer of Lieb-lattice M_2WS_4 (M = Fe/Mn/Co). **(b)**-**(f)** Calculated spin-resolved band structures of heterostructures formed by M_2WS_4 and various nonmagnetic monolayers, including PbO and PbS.

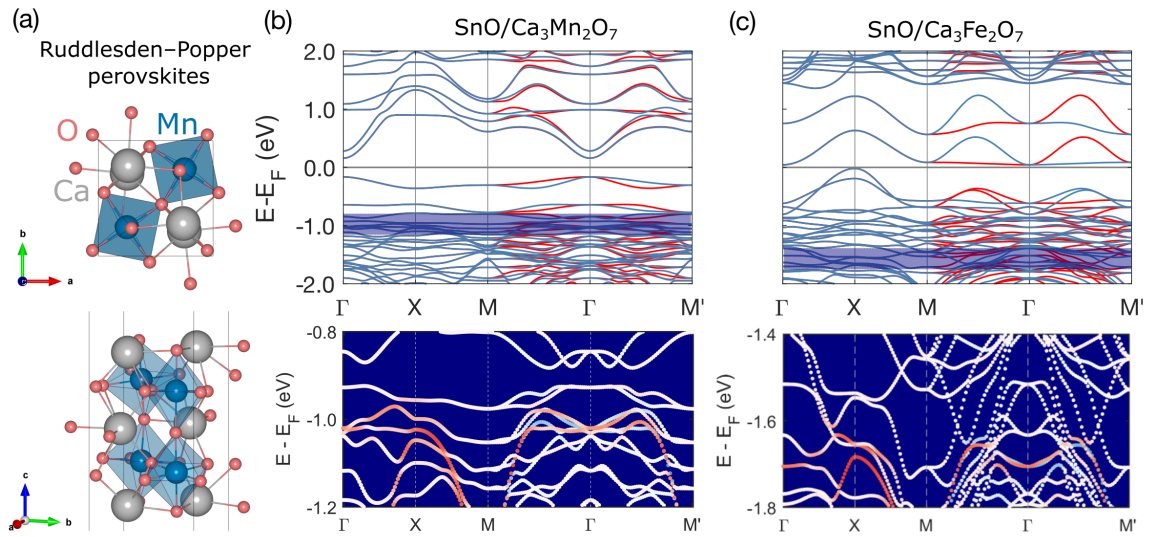

Fig. S7. **(a)**Crystal structure of the Ruddlesden-Popper perovskite $Ca_3Mn_2O_7$. **(b)** Calculated spin-resolved band structure of a heterostructure consisting of a SnO monolayer on a $Ca_3Mn_2O_7$ monolayer ($SnO/Ca_3Mn_2O_7$). **(c)** Same as **(b)**, but for the $SnO/Ca_3Fe_2O_7$ heterostructure. The lower panels highlight the SnO-derived bands, which exhibit proximity-induced altermagnetic spin splitting.

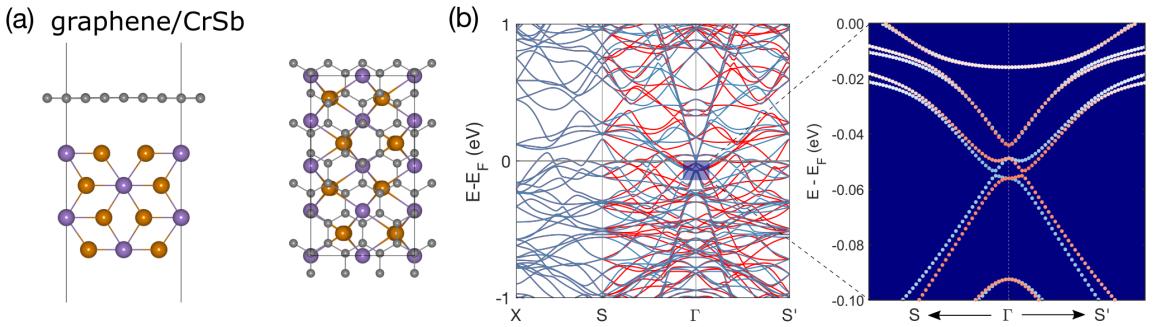

Fig. S8. **(a)** Crystal structure of the heterostructure formed by graphene on the CrSb (110) surface (graphene/CrSb). **(b)** Calculated spin-resolved band structure corresponding to **(a)**, together with a magnified view of the region near the Dirac point of the proximitized graphene.

Taken together, these results demonstrate that AMPE is a general phenomenon that is not restricted to a specific material class, but instead applies broadly across van der Waals, perovskite, and metallic altermagnets, thereby reinforcing the universality of the proposed mechanism.

SECTION VI: STRAIN CONTROL OF VALLEY SPLITTING IN PAM

Figure S9 presents the band structures of the PbS/V_2Se_2O heterostructure under different uniaxial strain conditions. These results demonstrate that, in the nonmagnetic PbS layer, the combination of AMPE and strain engineering can induce spin splitting and valley polarization.

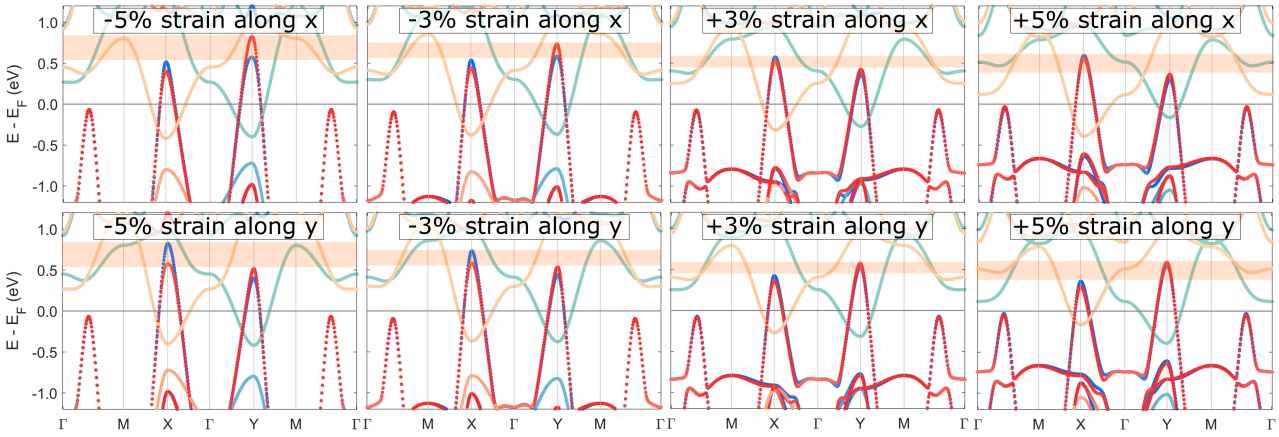

Fig. S9. Calculated band structures of the PbS/V_2Se_2O heterostructure under ±3% and ±5% uniaxial strain applied along the x and y axis. Red (spin-up) and blue (spin-down) denote the PbS component, while yellow (spin-up) and green (spin-down) represent the V_2Se_2O component.

SECTION VII: AMPE-INDUCED TOPOLOGICAL SUPERCONDUCTIVITY

The Bogoliubov–de Gennes (BdG) Hamiltonian for altermagentized $NbSe_2$ is given by

$$\begin{aligned} H_{BdG} = &\left(t_x \cos k_x + t_y \cos k_y - \mu\right)\sigma_0\tau_z \\ &+\lambda_R\left(\sin k_y\sigma_x - \sin k_x\sigma_y\right)\tau_z \\ &+J_A\left(\cos k_x - \cos k_y\right)\sigma_z\tau_0 + \Delta\sigma_0\tau_x, \end{aligned}$$

Although time-reversal symmetry is broken, the combined $[C_2\|C_{4z}]$ symmetry preserved by the altermagnetic term forbids a nonzero Chern number [9]. However, the system retains an additional twofold rotational symmetry (spin and spatial), $C_{2z}H_{BdG}(k_x,k_y)C_{2z}^{\dagger} = H_{BdG}(-k_x,-k_y)$ with $C_{2z} = \sigma_z\tau_0$, which allows the definition of Z_2-valued weak topological indices (ν_x,ν_y) [9, 10]. These indices are expressed as

$$(-1)^{\nu_x} = \prod_{n=1}^{2}\xi_n(\mathbf{X})\xi_n(\mathbf{M}),$$

$$(-1)^{\nu_y} = \prod_{n=1}^{2}\xi_n(\mathbf{Y})\xi_n(\mathbf{M}),$$

where $\xi_n = \pm 1$ denotes the eigenvalue of the C_{2z} operator for the occupied (negative-energy) eigenstate at the rotational invariant momenta $\mathbf{k}_R \in \mathbf{X},\mathbf{Y},\mathbf{M}$, i.e., $C_{2z}\left|u_n\left(\boldsymbol{k}_R\right)\right\rangle = \xi_n\left(\boldsymbol{k}_R\right)\left|u_n\left(\boldsymbol{k}_R\right)\right\rangle$. Direct diagonalization of H_{BdG} and applying the C_{2z} to the eigenstates yields

$$E_1(\mathbf{M}) = -\sqrt{\Delta^2 + \left(\mu + t_x + t_y\right)^2}$$

$$E_2(\mathbf{M}) = -\sqrt{\Delta^2 + \left(\mu + t_x + t_y\right)^2}$$

$$E_3(\mathbf{M}) = \sqrt{\Delta^2 + \left(\mu + t_x + t_y\right)^2}$$

$$E_4(\mathbf{M}) = \sqrt{\Delta^2 + \left(\mu + t_x + t_y\right)^2}$$

$$
\begin{aligned}
C_{2z}\left|u_1\left(\mathbf{M}\right)\right\rangle &= -\left|u_1\left(\mathbf{M}\right)\right\rangle \\
C_{2z}\left|u_2\left(\mathbf{M}\right)\right\rangle &= \left|u_2\left(\mathbf{M}\right)\right\rangle \\
C_{2z}\left|u_3\left(\mathbf{M}\right)\right\rangle &= -\left|u_3\left(\mathbf{M}\right)\right\rangle \\
C_{2z}\left|u_4\left(\mathbf{M}\right)\right\rangle &= \left|u_4\left(\mathbf{M}\right)\right\rangle
\end{aligned}
$$

$$
\begin{aligned}
E_1(\mathbf{X}) &= -2J_A - \sqrt{\Delta^2 + \left(\mu + t_x - t_y\right)^2} \\
E_2(\mathbf{X}) &= 2J_A - \sqrt{\Delta^2 + \left(\mu + t_x - t_y\right)^2} \\
E_3(\mathbf{X}) &= -2J_A + \sqrt{\Delta^2 + \left(\mu + t_x - t_y\right)^2} \\
E_4(\mathbf{X}) &= 2J_A + \sqrt{\Delta^2 + \left(\mu + t_x - t_y\right)^2}
\end{aligned}
$$

$$
\begin{aligned}
C_{2z}\left|u_1\left(\mathbf{X}\right)\right\rangle &= \left|u_1\left(\mathbf{X}\right)\right\rangle \\
C_{2z}\left|u_2\left(\mathbf{X}\right)\right\rangle &= -\left|u_2\left(\mathbf{X}\right)\right\rangle \\
C_{2z}\left|u_3\left(\mathbf{X}\right)\right\rangle &= \left|u_3\left(\mathbf{X}\right)\right\rangle \\
C_{2z}\left|u_4\left(\mathbf{X}\right)\right\rangle &= -\left|u_4\left(\mathbf{X}\right)\right\rangle
\end{aligned}
$$

$$
\begin{aligned}
E_1(\mathbf{Y}) &= -2J_A - \sqrt{\Delta^2 + \left(\mu - t_x + t_y\right)^2} \\
E_2(\mathbf{Y}) &= 2J_A - \sqrt{\Delta^2 + \left(\mu - t_x + t_y\right)^2} \\
E_3(\mathbf{Y}) &= -2J_A + \sqrt{\Delta^2 + \left(\mu - t_x + t_y\right)^2} \\
E_4(\mathbf{Y}) &= 2J_A + \sqrt{\Delta^2 + \left(\mu - t_x + t_y\right)^2}
\end{aligned}
$$

$$
\begin{aligned}
C_{2z}\left|u_1\left(\mathbf{Y}\right)\right\rangle &= -\left|u_1\left(\mathbf{Y}\right)\right\rangle \\
C_{2z}\left|u_2\left(\mathbf{Y}\right)\right\rangle &= \left|u_2\left(\mathbf{Y}\right)\right\rangle \\
C_{2z}\left|u_3\left(\mathbf{Y}\right)\right\rangle &= -\left|u_3\left(\mathbf{Y}\right)\right\rangle \\
C_{2z}\left|u_4\left(\mathbf{Y}\right)\right\rangle &= \left|u_4\left(\mathbf{Y}\right)\right\rangle
\end{aligned}
$$

Without loss of generality, we assume $J_A > 0$. Then taking the products of ξ_n for states with $E_n < 0$, we obtain

$$
\begin{aligned}
\nu_x &= \begin{cases} 1, & 2J_A > \sqrt{(\mu + t_x - t_y)^2 + \Delta^2}, \\ 0, & 2J_A < \sqrt{(\mu + t_x - t_y)^2 + \Delta^2}, \end{cases} \\
\nu_y &= \begin{cases} 1, & 2J_A > \sqrt{(\mu - t_x + t_y)^2 + \Delta^2}, \\ 0, & 2J_A < \sqrt{(\mu - t_x + t_y)^2 + \Delta^2}. \end{cases}
\end{aligned}
$$

A nontrivial index $\nu_{x/y} = 1$ indicates the emergence of a pair of chiral Majorana modes (CMM) at the corresponding edges, arising from band inversion at **X** / **Y**. Owing to the $[C_2 \| C_{4z}]$ symmetry of altermagnetism, the CMM associated with the **X** and **Y** valleys possess opposite chirality. Consequently, when $(\nu_x, \nu_y) = (1, 1)$, helical Majorana modes (HMM) emerge, and a valley-selective topological transition can be induced by breaking the crystalline isotropy ($t_x \neq t_y$). The phase diagram presented in the main text is obtained by substituting the corresponding parameters.

Our model represents a minimal phenomenological description of $NbSe_2$ proximitized by the altermagnetic material V_2Se_2O. Experimentally, the natural energy scale for such superconducting heterostructures is the pairing gap Δ. Here for $NbSe_2$, $\Delta \approx 1$ meV [11]. In our numerical calculations, the altermagnetic field J_A is 2Δ, i.e., 2 meV while the chemical potential $\mu \approx 3$ meV. Based on the topological invariants we obtained, the topological phase is achieved as long as $2J_A > \sqrt{\mu \pm (t_x - t_y)^2 + \Delta^2}$.

Our DFT-calculations indicate that the altermagnetic spin splitting is on the order of 10 meV, well above the minimum requirement. Therefore, the predicted topological phase should persist over a wide chemical-potential window extending tens

of meV, without fine tuning. While the Rashba SOC influences the magnitude of the superconducting gap and the indispensable effective $p-$wave pairing [12], it does not shift the phase boundaries. These considerations strengthen the experimental feasibility of observing the predicted Majorana modes.

* tzhou@eitech.edu.cn

[1] G. Kresse and J. Furthmüller, Efficient iterative schemes for ab initio total-energy calculations using a plane-wave basis set, Phys. Rev. B **54**, 11169 (1996).

[2] S. Grimme, Semiempirical GGA-type density functional constructed with a long-range dispersion correction, J. Comput. Chem. **27**, 1787 (2006).

[3] H. Ma, M. Hu, N. Li, J. Liu, W. Yao, J. Jia, and J. Liu, Multifunctional antiferromagnetic materials with giant piezomagnetism and noncollinear spin current, Nat. Commun. **12**, 2846 (2021).

[4] R. Xu, Y. Gao, and J. Liu, Chemical design of monolayer altermagnets, Natl. Sci. Rev. **13**, nwaf528 (2025).

[5] X. Xu and L. Yang, Alterpiezoresponse in two-dimensional lieb-lattice altermagnets, Nano Lett. **25**, 11870 (2025).

[6] L. Šmejkal, J. Sinova, and T. Jungwirth, Emerging research landscape of altermagnetism, Phys. Rev. X **12**, 040501 (2022).

[7] M. Gu, Y. Liu, H. Zhu, K. Yananose, X. Chen, Y. Hu, A. Stroppa, and Q. Liu, Ferroelectric switchable altermagnetism, Phys. Rev. Lett. **134**, 106802 (2025).

[8] Z. Zhou, X. Cheng, M. Hu, R. Chu, H. Bai, L. Han, J. Liu, F. Pan, and C. Song, Manipulation of the altermagnetic order in CrSb via crystal symmetry, Nature **638**, 645 (2025).

[9] D. Zhu, D. Liu, Z.-Y. Zhuang, Z. Wu, and Z. Yan, Field-sensitive dislocation bound states in two-dimensional d-wave altermagnets, Phys. Rev. B **110**, 165141 (2024).

[10] L. Fu and C. L. Kane, Topological insulators with inversion symmetry, Phys. Rev. B **76**, 045302 (2007).

[11] S. Kezilebieke, M. N. Huda, V. Vaňo, M. Aapro, S. C. Ganguli, O. J. Silveira, S. Głodzik, A. S. Foster, T. Ojanen, and P. Liljeroth, Topological superconductivity in a van der Waals heterostructure, Nature **588**, 424 (2020).

[12] M. Amundsen, J. Linder, J. W. A. Robinson, I. Žutić, and N. Banerjee, Colloquium: Spin-orbit effects in superconducting hybrid structures, Rev. Mod. Phys. **96**, 021003 (2024).